Volume 2 | Number 3 | May 2015 | Pages 255–352

Materials Horizons

rsc.li/materials-horizons

ISSN 2051-6347

ROYAL SOCIETY OF CHEMISTRY

COMMUNICATION

Bettina V. Lotsch *et al.*

Bringing one-dimensional photonic crystals to a new light: an electrophotonic platform for chemical mass transport visualisation and cell monitoring

Materials Horizons

COMMUNICATION

View Article Online
View Journal | View Issue

Cite this: *Mater. Horiz.*, 2015, **2**, 299

Received 8th October 2014
Accepted 6th January 2015

DOI: 10.1039/c4mh00195h

rsc.li/materials-horizons

Bringing one-dimensional photonic crystals to a new light: an electrophotonic platform for chemical mass transport visualisation and cell monitoring†

Ida Pavlichenko,[ab] Ellen Broda,[b] Yoshiyuki Fukuda,[c] Katalin Szendrei,[ab] Anna Katharina Hatz,[b] Giuseppe Scarpa,[d] Paolo Lugli,[de] Christoph Bräuchle[be] and Bettina V. Lotsch*[abe]

Photonic sensor technologies represent an important milestone in monitoring complex physical, chemical and biological systems. We present an integrated chemo- and bio-photonic sensing scheme drawing on the integration of one-dimensional (1D) stimuli-responsive photonic crystals (PCs) with an electrophotonic visualisation platform. We demonstrate various *modi operandi*, including the real-time mapping of spatial concentration distribution of a chemical analyte and the *in situ* monitoring of adhesive cell cultures, enabled by the modular combination of stimuli-responsive 1D PCs with various light emitters and detectors.

Conceptual insights

Recent progress in the development of numerous photonic crystal (PC) architectures along with a variety of state-of-the-art organic and inorganic light emitting devices and photodetectors covering a broad range of wavelengths has opened up new avenues in the photonic sensor technologies. In particular, one-dimensional (1D) PCs provide facile yet effective optical label-free detection schemes for a broad range of applications including environmental monitoring, industrial process control, food safety and others. In this work we endeavour to further expand the scope of integrated, 1D-PC-based sensing schemes and present an innovative electrophotonic sensing platform based on tunable 1D PCs, aiming for reduced cost and energy consumption, miniaturisation, high sensitivity, straightforward data processing and fast response times. By combining different types of light sources and detection schemes, we realise "smart" photonic crystals acting as optical transducers for spatially resolved refractive index changes and as platforms to probe macroscopic bio-objects on photonic surfaces. We address the possibility to perform real-time analysis of wetting and spreading kinetics and lateral spatial distribution of analytes adsorbed within porous multilayer structures, which can be of fundamental interest for the optical visualization of diffusion and pore-scale fluidic processes in photonic multilayer systems. Additionally, a non-invasive, real-time optical monitoring approach for evaluating the confluency and viability of unlabelled fibroblast- and tumorigenic hepatocyte-type cells adhered to a biocompatible 1D PC surface is presented, which can be of interest for future cancer progression studies and for drug toxicity and pathogenicity tests.

Introduction

Since their conception in 1987, photonic crystals have transformed into one of the most versatile classes of optical materials, particularly in the realm of sensing.[1–4] PCs are artificial nanostructures capable of molding the flow of light in one, two or three dimensions due to their unique ability to guide, restrict or block the motion of photons, which originates from the periodic variation of the dielectric constant of the media comprising the PC.[5] Well-defined physical properties together with tailored chemical functionalities of the PCs have empowered their use in label-free colorimetric sensing platforms capable of fast and reliable ambient monitoring.[6,7] Devices that spotlight facile coupling to the photonic nano- and microstructures aim for a simplified read-out, robust *modus operandi*, large-scale and low-cost production and straightforward and accurate data processing recipes.[8,9] Sensing devices featuring an *electrophotonic* transduction scheme exploit the integration of a PC with an optoelectronic detection scheme, thus allowing to read out the *photonic* response of a stimuli-responsive PC *electronically* without utilising a spectrophotometer (as in the traditional colorimetric approach).[10] This concept does not only provide a highly sensitive and compact read-out, but simultaneously allows for interfacing the detection panel with micro- and nanofluidic dosing or sequencing systems for the development of integrated, portable "lab-on-a-chip" platforms.[11–13] Furthermore, implementing the electrophotonic transduction scheme in the development of compact visualisation platforms capable of time and spatially resolving dynamic processes such

[a]*Max Planck Institute for Solid State Research, Heisenbergstrasse 1, 70569 Stuttgart, Germany. E-mail: b.lotsch@fkf.mpg.de*

[b]*Department of Chemistry, Ludwig Maximilian University (LMU), Butenandtstrasse 5-13 (D), 81377 Munich, Germany*

[c]*Max Planck Institute of Biochemistry, Am Klopferspitz 18, 82152 Martinsried, Germany*

[d]*Institute of Nanoelectronics, Technical University of Munich, Arcisstrasse 21, D-80333 Munich, Germany*

[e]*Nanosystems Initiative Munich (NIM) and Center for NanoScience, Schellingstraße 4, 80799 Munich, Germany*

† Electronic supplementary information (ESI) available. See DOI: 10.1039/c4mh00195h

as thermal mapping, vapour and liquid diffusion, cellular adhesion and proliferation, and others can be key for enhanced environmental sensing, point-of-care diagnostics and biosecurity technologies.

En route with the advancement of PC-based sensors meeting the aforesaid requirements, a myriad of colorimetric and fluorometric platforms for vapour and liquid analysis have been designed, which are referred to as artificial noses.[2,14,15] Such platforms allow for a better discrimination between individual compounds in mixtures as compared to the traditional costly gas chromatography-mass spectrometry tandems.[16] An optofluidic nose based on the combinatorial "wetting in color kit" (WICK) comprising 3D PCs – surface-modified silica inverse-opal films – has been introduced recently by Burgess *et al.*[17] WICK allows for encoding chemical information *via* unmasking visible patterns by exposure to substances with various surface tensions.[18] Photonic porous silicon (PSi) nanostructures have also proven to be versatile tools for chemo- and biosensing.[19–23] A single component optical "nose" based on stacked PSi rugate photonic crystals capable of identifying organic vapours at parts-per-million (ppm) concentrations *via* time-resolved diffusion drift analysis was suggested by Kelly *et al.*[24] In terms of cell monitoring, a number of photonic crystal-inspired visualisation platforms have been developed recently.[25] The need for quantitative, time-resolved analysis of a multitude of vital cellular processes, such as cell differentiation, chemotaxis, apoptosis, metastasis, wound healing, cell surface attachment and others without sample pre-fixing has sparked the development of an imaging technique known as photonic crystal enhanced microscopy (PCEM).[26,27] Cunningham and co-workers showed that label-free imaging of cell attachment on low-refractive-index sub-wavelength guided mode resonant (GMR) gratings is possible with 0.61 μm^2 resolution.[26] Likewise, Nazirizadeh *et al.* have demonstrated that the combination of GMR spectral mapping of a 1D photonic crystal slab with finite-difference time-domain (FDTD) simulations of the GMR allows translating the 2D real-time bright-field images into 3D topography of the adhered cells in a non-invasive fashion.[28]

Among the various PC architectures for sensing applications, 1D PCs – multilayer structures with a periodic modulation of the refractive index (RI) in one dimension referred to as Bragg stacks – are of particular practical relevance due to their low complexity as well as straightforward and inexpensive wet-chemistry-based fabrication methods. A facile optical read-out is provided by the photonic band gap (PBG), a forbidden frequency range between the air and dielectric bands, which is analogous to a band gap between the conduction and valence bands in electronic semiconductors. Favorably, the position and shape of the PBG can be modulated by changing the lattice constant and/or the dielectric contrast of the materials constituting the PC by various external stimuli, which facilitates their application in physical, chemical and biological sensors.[29–32] In spite of the abundance of material combinations available for the fabrication of 1D PCs, the prototype materials titanium dioxide and silicon dioxide offer a range of advantages for the assembly of high-quality multifunctional multilayers, including high RI contrast, nanomorphology and surface chemistry-based modification possibilities, high chemical and mechanical stability, biocompatibility and self-cleaning properties of TiO_2.[33–35] Along these lines, Bonifacio *et al.* have realised a photonic nose biosensor by chemically "pixelating" nanoparticle-based (NP-based) TiO_2/SiO_2 stacks capable of displaying the optical fingerprints of various bacteria strains.[36,37] To address the demand for label-free, fast and reliable monitoring systems featuring an optical read-out, we have recently demonstrated an integrated "electrophotonic nose" sensing platform based on a stimuli-responsive NP-based TiO_2/SiO_2 1D PC as a sensing element integrated with an organic light-emitting diode (OLED) as light source and an organic photodetector (OPD) as light detector, which is capable of detecting ppm concentrations (down to $\approx$10 ppm) of organic solvents with a fast performance comparable to the one of modern state-of-the-art breathalysers (response time of $\approx$2.6 s for a change in ethanol gas concentration of 100 ppm).[13]

In this work we aim to further expand the scope of integrated, 1D-PC-based sensing schemes, discuss important aspects of sensor design, and present new operational modes of the photonic-to-electronic sensing approach in chemo- and biosensing, with a particular focus on chemical diffusion mapping and cell monitoring. The promising novel sensing applications arising from the integration of stimuli-responsive NP-based TiO_2/SiO_2 1D photonic crystals with various light emitting devices and photodetectors represent a central "three-in-one" motif of our study. We discuss possible advantages of the photonic-to-electronic signal transduction scheme based on the judicious choice of the light source bandwidth – broadband, narrowband or monochromatic. We demonstrate the possibility to perform direct analysis of the spatial distribution of analytes adsorbed within porous multilayers with micrometre resolution by combining a 1D PC with broadband and narrowband light emitters and imaging arrays, which can be of great interest in many applications including photovoltaics, (barrier) membranes, drug delivery systems and others.[38,39] Additionally, we have visualised the lateral mass transfer of the analyte into porous multilayers associated with wetting and imbibition, which plays an important role in various ubiquitous phenomena including the "coffee ring effect", and in industrial applications, such as cooling technologies, ink-jet printing and 3D-printing.[40,41] Furthermore, by measuring the change in the light power signal of a monochromatic light source modulated by a 1D-PC-cell hybrid structure, we demonstrate a non-invasive, real-time, optical monitoring approach for evaluating the confluency and viability of unlabelled cells adhered to a 1D PC surface. We show the possibility to rapidly test cytotoxic effects induced by certain chemicals of interest by using the example of fibroblast surfactant-induced lysis. Furthermore, we highlight the potential of the photonic-to-electronic platform in assessing cell proliferation on the PC surface, by monitoring the coverage of human hepatocarcinoma cells.

Results and discussion

A comprehensive overview of the functionalities provided by the proposed sensing platform is schematically shown in Fig. 1. As

can be seen, the sensing platform is composed of three major components: a stimuli-responsive optical element – the 1D photonic crystal –, a photodetector (spectrometer, organic/inorganic photodiode or an imaging array), and *a light source* (LS). Importantly, the latter is categorised into three classes of light emitters based on their bandwidth – namely, broadband (*e.g.* incandescent lamp), narrowband (*e.g.* LED and OLED), and monochromatic (*e.g.* laser) LSs. Depending on the LS used, the presented "sandwich-like" sensing setup allows for the three modes of read-out referred to in Fig. 1 as "spectral tuning", "intensity tuning" and "imaging". Specifically, in the "spectral tuning" mode the classical spectroscopic read-out of the optical response of a color-tunable PC is realised – the spectral shift of the PBG induced by an external stimulus is recorded by a spectrometer in the chosen wavelength range. The next mode is "intensity tuning", in which one can tune the initial emission intensity of the light source by tuning the band gap of a responsive 1D PC and register the optical response with a photodiode or radiometer. This transduction scheme can, in principle, be realised with all three types of the above-named LSs, however, it is more straightforward to tune the intensity of narrowband and monochromatic LSs: one can deliberately design a 1D PC with tailor-made optical properties for the optimal tuning of a LS in a specific (narrow) range of wavelengths, matching the responsivity range of the chosen detector. The position of the central wavelength of the PBG should be chosen such that the "blue" or "red" PBG slope corresponds with the maximum emission wavelength of the LS (as shown in the schematic insets in Fig. 1). Finally, the third mode – "imaging" – is realised by integrating the 1D PC with an imaging array, such as a charge-coupled device (CCD) or a complementary metal-oxide semiconductor (CMOS) camera, and either reading out the color of the PC with a color camera, or recording the intensity change with a grayscale camera, using the "spectroscopic" or "intensity" tuning approaches mentioned afore. Below we will provide a comparative study of the presented measurement modes as well as shed light on the new application possibilities enabled by integrating 1D PCs with various light sources and detectors.

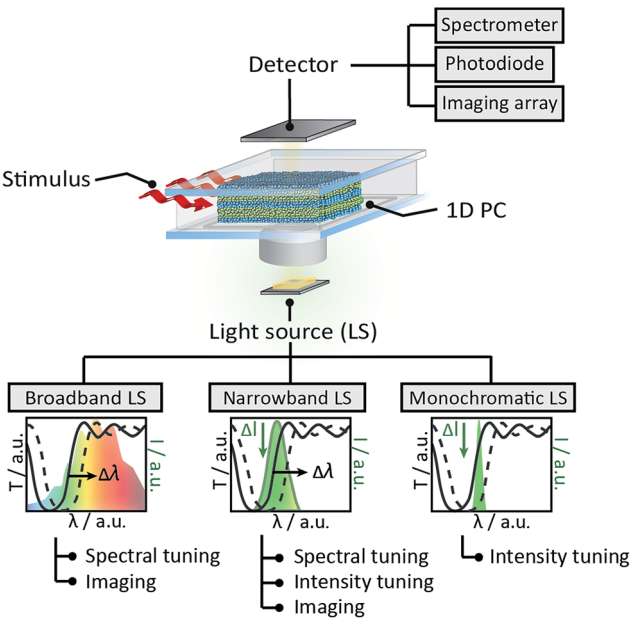

Fig. 1 Schematic illustration of the suggested sensing platform featuring a stimuli-responsive 1D PC as the sensitive element, and overview of the different measurement modalities enabled by various light sources (broadband, narrowband and monochromatic LSs) and photodetectors (spectrometer, photodiode and imaging arrays).

Firstly, we discuss previously unexplored prospects of interfacing the responsive 1D PCs with a spectrometer and imaging array to enable temporal and spatial observation of chemical adsorption/desorption processes within the 1D PC. We combine the stimuli-induced spectral tuning of the PBG, enabled by illumination with a broadband halogen lamp light source, with the quantitative analysis of the true-color images of the 1D PC obtained with an imaging array, to gain information about the spatial concentration of the analyte during the diffusion process. To perform the above-mentioned spectral characterisation of the chosen 1D PC (as shown in Fig. 2), the ethanol vapour was mixed with a N_2 carrier gas at various concentrations to achieve relative vapour pressures from 0 to 100% and continuously delivered to a polydimethylsiloxane (PDMS) chamber sandwiched between the 1D PC surface and the glass slide window (see the ESI† for a description of the experimental procedure). The 1D PC surface was exposed to a vapour volume of $\approx 2 \times 2 \times 0.4$ cm^3 provided by the chamber. The 1D PC was composed of 9 bilayers of porous TiO_2 ($\approx$90 nm) and SiO_2 ($\approx$135 nm) nanoparticle layers, starting with a SiO_2 layer and finishing with TiO_2. Fig. 2a depicts a SEM cross-section micrograph of the multilayer system, showing the TiO_2 layer as bright stripes and the SiO_2 as dark stripes (the fabrication routine is provided in the ESI†). The refractive index (n_D^{20}) of porous single films was determined *via* spectroscopic ellipsometry at 20 °C as a function of ethanol relative pressure for TiO_2 ($n_D^{20}(0\%) = 1.875$, $n_D^{20}(100\%) = 1.915$) and SiO_2 ($n_D^{20}(0\%) = 1.325$, $n_D^{20}(100\%) = 1.385$) films placed into the closed chamber. As can be seen in Fig. 2b, the PBG shifts towards longer wavelengths by $\approx$55 nm without a loss in reflectivity ($\approx$95%) upon increasing the relative pressure of the ethanol vapour from 0 to 100%. By extracting the wavelength values corresponding to 60% of the reflectance for various p/p_0 (shown with a red arrow in Fig. 2b) we obtain the optical isotherm of the vapour adsorption – the spectral shift as a function of the relative vapour pressure – as shown in Fig. 2c. The shape of the optical adsorption isotherm corresponds to a type IV isotherm, indicating capillary condensation of the gas molecules in the textural mesopores of the materials.[42] We have also analysed the response time of the 1D PC in Fig. 2a to changes of relative ethanol vapor pressure from 0% to 20%, from 0% to 50% and from 0% to 100% (corresponding to the initial concentration change of ethanol molecules in the chamber of $\approx$12 800, 32 000 and 64 000 ppm, respectively) (see ESI, Fig. S1†). The measured time response of the nanoparticle-based 1D PC to a p/p_0 change were 9.2 s, 4.0 s and 5.1 s, respectively.

Next, we discuss the lateral mass transport in a porous medium, particularly during evaporation, and demonstrate the

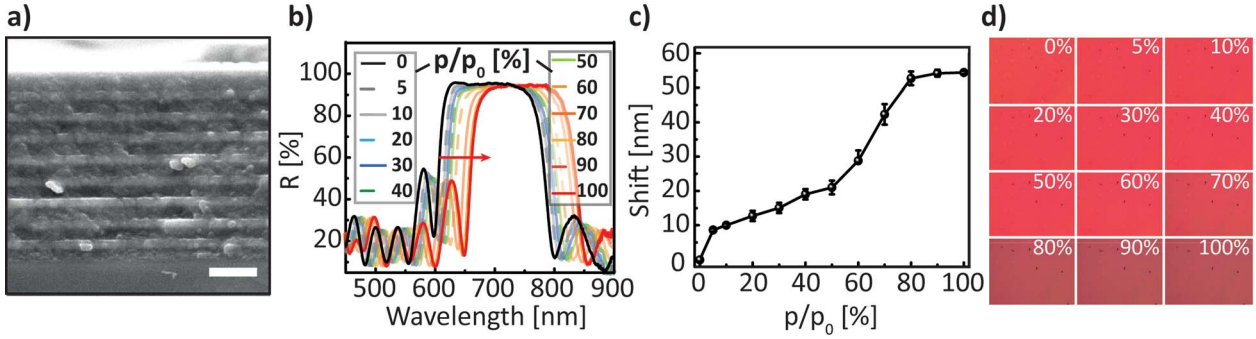

Fig. 2 (a) Cross-section SEM image of the investigated 1D PC, composed of 9 nanoparticle-based SiO_2 (darker layers ≈ 135 nm)/TiO_2 (brighter layers ≈ 90 nm) bilayers, scale bar is 0.5 μm; (b) reflectance spectra of a TiO_2/SiO_2 1D PC at normal incidence show a red shift (≈55 nm) upon infiltration with ethanol vapour at p/p_0 from 0 to 100%; (c) optical isotherm for the adsorption branch of the ethanol vapour; (d) photographs of the 1D PC surface captured during the acquisition of the spectra shown in Fig. 2b at various p/p_0.

possibility of directly visualizing the lateral spatial distribution of ethanol in the porous multilayer system. The results obtained in the following paragraph are directly interrelated with the characterisation of the 1D PC made in Fig. 2. Namely, in parallel with the spectral acquisition shown in Fig. 2b, photographs of the 1D PC surface in RGB color space were captured with the CMOS image sensor covered with a RGB Bayer mosaic filter. Images were taken for the corresponding relative pressure values after 120 s of equilibration; p/p_0 values are indicated in the upper right corner of the individual image, as shown in Fig. 2c. The photographs shown in Fig. 2d were further converted into grayscale color space for calibration purposes. To perform the calibration, the relative luminance (Y) depending on the spectral sensitivity of human visual perception of brightness was calculated by using eqn (1), which includes the weighing of the three stacked colour channels – red (R), green (G) and blue (B):

$$Y = 0.299R + 0.587G + 0.114B. \quad (1)$$

For a clear and fast visual representation of the lateral mass transport in the porous multilayer system we used a model experiment of spreading/evaporating a liquid ethanol droplet. For liquid droplets on porous substrates several classical wetting states can be observed:[41] (i) Cassie–Baxter state, in which the liquid does not penetrate into the pores; (ii) Wenzel state, in which the liquid wets the pores only directly under the droplet; and (iii) Cassie–Baxter impregnating wetting state, in which the liquid wets the pores not only directly under the droplet, but also beyond the contact line (see the inset of Fig. 3a). At the beginning of the experiment a 3 μL droplet of liquid ethanol was carefully placed on the surface of the porous 1D PC, whose sorptive properties were already discussed in Fig. 2b–d; note that for the experiment the 1D PC was also placed into the closed PDMS chamber with a glass window as in the previous experiment (Fig. 2b–d).

To keep the experimental conditions the same, the chamber was ventilated by a slow laminar N_2 gas flow of 50 mL min^{-1}. Upon injecting the droplet onto the porous surface of the 1D PC one can observe that the droplet spreads fast with an axisymmetric profile until it reaches the maximum size, and at the same time normal and lateral imbibition of the liquid takes place causing a volume loss of the droplet and the decrease in contact angle, corresponding to Cassie–Baxter impregnating wetting behavior[41,43] (iii); simultaneously the wetted region *within* the multilayer expands; afterwards the droplet and the imbibed liquid evaporate from the surface of the 1D PC and concurrently also from the porous network of the multilayer. From the evolution of dynamic contact angle (DCA) of the ethanol at the droplet base shown in Fig. 3a one can see that the DCA changes rapidly (within 2 s) over an initial stage of spreading and then remains relatively constant reaching a value of 21.5 ± 0.3°, which is in agreement with the theory of Starov *et al.*[43] for spreading of liquids on porous substrates. The dynamic process of spreading, penetration and evaporation of the liquid ethanol droplet was visualised by using the CMOS image sensor with the same settings as in the previous experiment (shown in Fig. 2) to enable the correct post-processing. The obtained data was further used to serve two major purposes: (a) to analyse the kinetics of the lateral mass transport during the evaporation stage and (b) to visualise the lateral spatial distribution of analyte in the multilayer – both (a) and (b) during the evaporation stage. To analyse (a) – the kinetics of the evaporation – we used the $Y(x,y,t)$ matrices obtained in Fig. 3b for the assembly of a kymograph (a time-space plot, see Fig. 3c), which allows for the visual representation of the following processes: (I) visualization of the dry 1D PC, (II) ethanol injection, (III) ethanol spreading/imbibition, (IV) evaporation from the surface of the 1D PC (note the moving thin-film interference pattern), (V) evaporation of the imbibed area from the porous network of the 1D PC, and (VI) state where ethanol is completely evaporated. By extracting the luminance profile $Y(t)$ in the area of interest (evaporation stage "V") in the kymograph as shown in Fig. 3d, one can assess the time needed for a complete evaporation (≈6 s) and obtain the power law scaling dependence for relative luminance of $Y \sim t^{0.17}$ by fitting the evaporation curve shown along the thick grey dashed line in Fig. 3d. For the second purpose (b), *i.e.* the visualisation of the lateral spatial distribution during ethanol evaporation (see Fig. 3e–h), the true-color photographs taken at normal incidence,

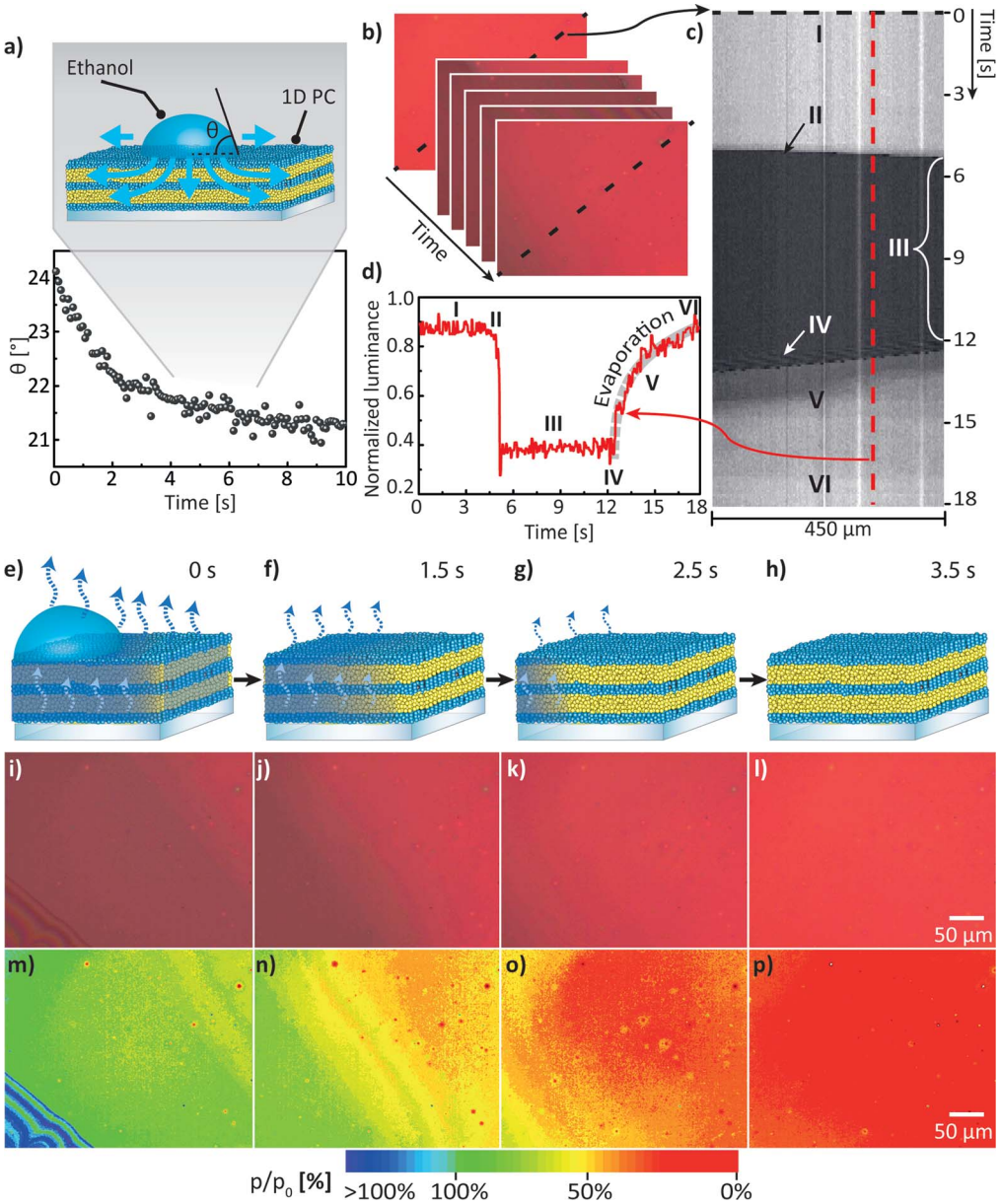

Fig. 3 (a) Evolution of the mean contact angle measured at the base of a 3 µL ethanol droplet spreading on a surface of the 1D PC. The inset schematically shows the transport phenomena for a droplet in the Cassie–Baxter impregnating wetting state placed onto porous substrate. (b) An area of ≈0.1 mm^2 exposed to ethanol spreading and evaporation was recorded and converted into a set of time-dependent RGB frames and afterwards into grayscale relative luminance matrices ($Y(x,y,t)$), (c) the relative luminance profiles along the diagonal of 450 µm in length (shown with a dashed line in b) were extracted for each frame (time point) and assembled into a kymograph, which was then normalised with respect to the highest intensity value. Six areas can be distinguished on the kymograph (c): (I) 1D PC in the dry state, (II) liquid injection, (III) spreading and imbibition of liquid followed by evaporation (IV) from the surface of the 1D PC (note the striped interference pattern characteristic for thin films) and (V) from the (imbibed) porous network of the 1D PC, and, finally, (VI) complete evaporation of ethanol. For further analysis $Y(t)$ profile was extracted along the dashed red line in the kymograph (c) for the corresponding areas (I–VI) and plotted in (d) to show the kinetics of evaporation from the porous network (highlighted with a thick dashed grey line in the area "V"). (e–h) Visualization of chemical mass transport in a 1D PC during droplet spreading and imbibition: schematic illustration of the analyte droplet (*e.g.* ethanol) evaporating from the surface of the 1D PC, followed by evaporation of the analyte from the porous network of the multilayer at (e) 0 s, (f) 1.5 s, (g) 2.5 s and (h) 3.5 s after the start of the acquisition. (i–l) show the CMOS true-color photographs taken normally to the 1D PC surface during ethanol evaporation at (i) 0 s, (j) 1.5 s, (k) 2.5 s and (l) 3.5 s. (m–p) show the corresponding calibrated time-resolved pseudo-color maps of the ethanol relative pressure distribution during the evaporation process.

depicting a 300 µm^2 area of the 1D PC, were analysed (Fig. 3i–l). By taking into account that the images in Fig. 2d allowed for establishing a calibration relation ($Y(p/p_0)$) between the relative luminance value and the known relative pressure, the true-color photographs in Fig. 3i–l can be transformed into the two-dimensional calibrated pseudo-color maps of the ethanol

relative pressure distribution during the evaporation process as shown in the Fig. 3m–p. Specifically, by comparing the values of the relative pressure in the pseudo-color maps in Fig. 3m–p one can see that in the beginning of the evaporation process the vicinity of the droplet (an annular sector with an area of ≈0.075 mm^2) is fully impregnated with ethanol (green tints corresponding to p/p_0 of ≈90–100%), while already after 1.5 s a smaller sector of the 1D PC (area of ≈0.038 mm^2) corresponds to relative pressures of 75–90%; after 2.5 s ethanol approximately 0.010 mm^2 of the area of observation was at (p/p_0 of ≈45–65%), and after 3.5 s ethanol has fully desorbed from ≈95% of the area of observation (as derived from the red coloration). Thus, we have shown that the mass transport processes in a multilayer 1D PC system can be visualised and quantified in a time-resolved fashion based on a photonic read-out, revealing the spatial concentration distribution of the analyte condensed in the pores.

Having demonstrated the possibility to perform a quantitative analysis of mass transport maps *via* spectral tuning and imaging, in the next step we extend the capabilities of our sensing platform by introducing the second read-out mode, namely intensity tuning through an "electrophotonic nose" array (see Fig. 1). To this end, we have replaced the broadband LS used in the previous measurements in Fig. 2 by its narrowband analogue with a bandwidth of ≈100 nm. The experimental setup for the electrophotonic sensing platform is schematically depicted in Fig. 4a, and the photograph of a prototype setup is shown in Fig. 4b. The platform encompasses a tunable 1D PC placed into the closed PDMS chamber with a glass window and a volume of 1.6 cm^3, with built-in inlet and outlet for the analyte of interest (in gaseous and liquid phases), a narrowband LS (≈100 nm wide green LED centered at 550 nm) and the photodetector (*e.g.* a power sensor and/or the CMOS imaging array). For the chemical adsorption and diffusion experiments shown in Fig. 4 we have modified the architecture of the 1D PC from the one used in Fig. 2, to align the photonic bandgap with the emission band of the LED. As mentioned previously,[13] optimisation of the layer thicknesses and RI contrast of the layers is needed in order to maximise the response of the 1D PC integrated with the LS of interest. The position of the PBG was chosen such that the steepest slope of the longer wavelength side (dielectric band) of the PBG lies in a range of 540–560 nm. To meet this criterion, we have fabricated the 1D PC with 6 bilayers of SiO_2 (≈90 nm)/TiO_2 (≈60 nm) nanoparticle films, as can be seen in the cross-section SEM image shown in Fig. 4c. The RIs of the single films measured for 0 and 100% relative ethanol pressure are $n_D^{20}(0\%) = 1.839$ and $n_D^{20}(100\%) = 1.923$ for TiO_2 and $n_D^{20}(0\%) = 1.301$ and $n_D^{20}(100\%) = 1.355$ for SiO_2. Due to the nature of the experimental setup (see Fig. 4a and b) – the light from the LED is shone through the 1D PC from the bottom and analysed on the opposite side by a power sensor – we have collected the spectra in transmission mode for the spectral characterisation of analyte sorption. The response of the 1D PC to the change in relative ethanol pressure from 0 to 100% was first measured *via* the classical spectral tuning approach, see Fig. 4d: the PBG red shift (≈25 nm) was recorded in the wavelength range between 500 and 600 nm upon increasing the p/p_0 from 0 to 100%. The inset in Fig. 4d displays the corresponding optical adsorption isotherm, *i.e.* the dependence of the transmittance values extracted at 550 nm ($T_{550\ nm}$) on p/p_0. As seen in the inset of Fig. 4d, the convolution of the spectral properties of the LED and the tunable PC leads to a decrease in the intensity of the used LS: as the "red" PBG edge shifts towards longer wavelengths (due to the increased effective refractive index of the infiltrated layers) in the range between 500 and 600 nm, the transmittance ($T_{550\ nm}$) corresponding to the LED emission peak at 550 nm is decreasing, thus reducing the output LED intensity. This constellation was also independently proven in the photonic-to-electronic transduction experiment shown in Fig. 4e. For this, the modulated power of light was measured by means of a power sensor for various p/p_0. The measured values of the power range from 140 μW to 190 μW for the LED driven at 8 mA. Similar to the experimental routine described in Fig. 2d, in parallel with the spectra acquisition we have captured the photographs of the multilayer surface with a CMOS imaging array at $0 < p/p_0 < 100\%$ and performed a relative luminance analysis of the individual photographs (see ESI, Fig. S2†) for calibrating the diffusion gradient and mapping the spatial concentration of the analyte in the multilayer, as demonstrated in Fig. 4f. In the top part of Fig. 4f one can see the true-color photograph of the gradient concentration distribution of ethanol, depicted in transmission mode after 2 s from the start of the acquisition. The image appears green to the viewer due to the color of the LED. The corresponding calibrated pseudo-color 110 × 81 μm^2 map of the ethanol relative pressure distribution is displayed in the bottom part of Fig. 4f. It can be seen that after 2 s ethanol has evaporated from more than 60% of the observed PC area. Summarising the above experiments, one can conclude that in contrast to the broadband-LS-illuminated sensors featuring a colorimetric read-out as shown in Fig. 2, the use of narrowband LSs such as LEDs (and OLEDs) can enhance the sensing capabilities of the 1D PC platform by additionally providing a photonic-to-electronic read-out that allows for the design of highly compact, integrated sensors with high sensitivity in the whole range of relative pressures of the volatile analytes ($0 < p/p_0 < 100\%$). Besides, the analysis of sorption kinetics in 1D PCs integrated with narrowband light sources can also be performed with less expensive CMOS arrays without a RGB Bayer mosaic filter.

Hereafter, we address the last of the proposed read-out modes of our sensing platform – integration of the 1D PC with a monochromatic light source – to show the potential applicability of the electrophotonic platform for *in situ* cell monitoring. Monochromatic light is advantageous for its robustness against chromatic aberrations as well as long-term intensity stability and its collimated light beam. A schematic illustration of the cell analysis platform in Fig. 5a shows the 1D PC with the cell layer, placed into a Petri dish with the buffer. The input power of the monochromatic light source (for the presented experiments we used a 532 nm laser) is first modulated by the 1D PC, and then recorded by the Si photodiode power sensor. The photographs of the employed 1D PC taken normally and at an angle of ≈45° are shown in Fig. 5b and c (note that the ring

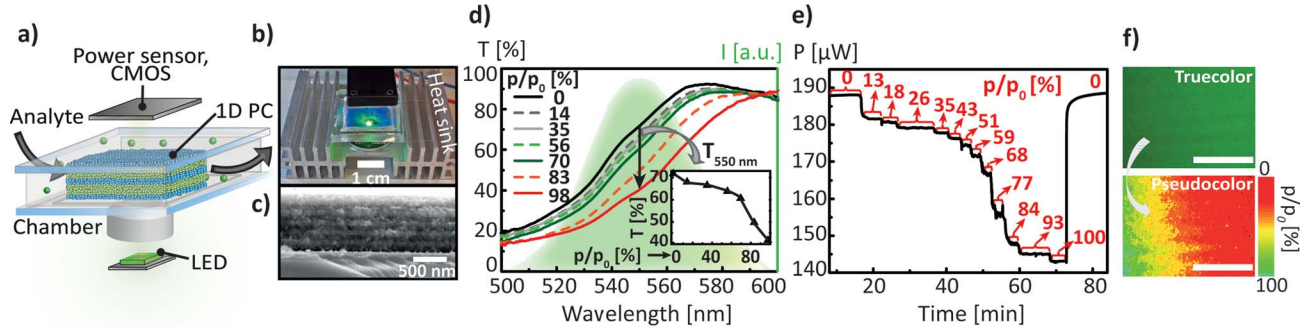

Fig. 4 (a) Schematic illustration of the electrophotonic platform for chemo-sensing depicts a narrowband light source shining through the tunable 1D PC located in the closed chamber, to which an analyte of interest is being delivered; (b) photography of a prototype platform based on a green LED with a wavelength band centered at 550 nm as a light source and a slim Si photodiode power sensor as a detector; (c) cross-section SEM image of the 1D PC, composed of 6 nanoparticle-based SiO_2 (≈90 nm)/TiO_2 (≈60 nm) bilayers, the scale bar is 500 nm. The response of 1D PC to the external stimulus can be measured *via* (d) the classical spectral analysis of the photonic stop band shift in the narrow range of wavelengths between 500 and 600 nm (provided by the LED), induced by the infiltration of the PC porous network with analyte (ethanol) at relative pressures (p/p_0) from 0 to 10%; the inset shows the dependence of the transmission values extracted at 550 nm on p/p_0, or *via* (e) the photonic-to-electronic transduction path by measuring the modulated power of light versus time for various p/p_0 by means of a power sensor, the p/p_0 values are indicated with the red arrows for each plateau region. (f) Visualization of the chemical analyte diffusion. Top: true-color photograph of the gradient concentration distribution of ethanol in the 1D PC illuminated by green light, bottom: the corresponding calibrated pseudo-color map of the ethanol relative pressure distribution, the scale bar is 50 μm.

defect in the middle of the substrate indicates a spin-coater chuck mark; this area was not used for the measurements). The large round samples were then divided into smaller pieces of about 5 mm^2. The PC was fabricated out of 6 NP-based bilayers starting with SiO_2 (≈90 nm) and finishing with a top TiO_2 (≈60 nm) layer, as displayed in the cross-section SEM micrograph in Fig. 5d. The thickness of the layers was optimised in order to match the position of the central wavelength of the PBG with the laser emission wavelength (532 nm). By applying the intermediate calcination routine to the individual NP-based SiO_2 and TiO_2 layers (see ESI†), we have obtained durable 1D PCs, possessing excellent mechanical stability upon long term exposure to fluids – the durability of the samples placed in water was up to three months and up to one month in the cell culture medium. For preliminary studies of the optical PC properties modified with adhesive cell lines we have used BHK-21 fibroblasts. In order to obtain the cell thickness distribution, we have investigated a topography of the fixed BHK-21 fibroblast monolayer on the 1D PC surface by AFM, as shown in Fig. 5f.

4% paraformaldehyde was chosen as an optimal fixative enabling good optical quality of the BHK-21 cells, preserving the fibroblastic morphology and preventing the presence of debris on the substrate.[44] The measured thickness of the cells fixed after 24 h of incubation ranges between 50 and 900 nm. Furthermore, the overlay fluorescence image of the fixed BHK-21 cells attached to the 1D PC after 24 h of incubation in Fig. 5g shows the distribution of TRITC-phalloidin dye ($\lambda_{emission}$ at ≈573 nm) in actin filaments, indicated by red color, and Hoechst-33342 ($\lambda_{emission}$ at ≈497 nm) in the double stranded DNA, indicated by blue color, proving that the cells remained adherent and viable on the PC surface. To estimate the impact of the adhered cell layer on the optical properties of the 1D PC, we have carried out simulations in Comsol Multiphysics RF Module.[45] Fig. 5g represents a comparison of the simulated transmittance spectra of the PBG of the 6 bilayer 1D PC (SiO_2 thickness of 90 nm; TiO_2 thickness of 60 nm) without the cell monolayer (black curve) and the PC covered with a 100% confluent cell layer with an effective thickness of 200 nm (the average cell thickness value determined from the AFM topographic map in the Fig. 5f) and a refractive index of 1.40 (ref. 46) (gray curve). The simulation was performed based on the assumption that the pores of the multilayer are filled with cell medium liquid ($RI_{eff/titania}$ = 1.35, $RI_{eff/silica}$ = 1.90). As a result, a significant decrease in transmittance by 7% measured at 532 nm (from 18% to 11%), due to the introduction of the cellular monolayer onto the PC, was predicted by our simulations. Consequently, one should expect a decrease in the laser signal shining through the PC covered with cells compared to the bare PC. Noteworthy, a similar decrease of 7.5% in the reflectance was reported for a porous SiO_2 Fabry–Pérot thin film upon immobilisation of an *E. coli* bacterial layer.[47] The experimental transmittance spectra of the used 1D PC with (gray line) and without (black line) the fixed BHK-21 cell layer are shown in Fig. 5h. The spectra were obtained for the PC immersed into 2 mL of transparent CO_2-independent cell medium (dashed lines, "M") and for the PC without cell medium (in ambient air) at relative humidity of 21% (solid lines, "NM"). Fig. 5h gives a visible explanation for the above-discussed choice of the lattice parameter and the morphology of the 1D PC. It can be clearly seen that upon filling the pores of the layers with the cell medium the effective refractive index of SiO_2 and TiO_2 increases and, thus, the spectrum (black solid and dashed lines) shifts by ≈55 nm towards longer wavelengths, such that the PBG matches with the emission peak of the laser at 532 nm. By comparing the spectra in Fig. 5g and h for the PC placed in the cell medium (dashed lines) with ("+") and without ("-") a cell layer, one can see a clear correlation between the simulated and the experimental plots. Similarly as the simulated curves, the

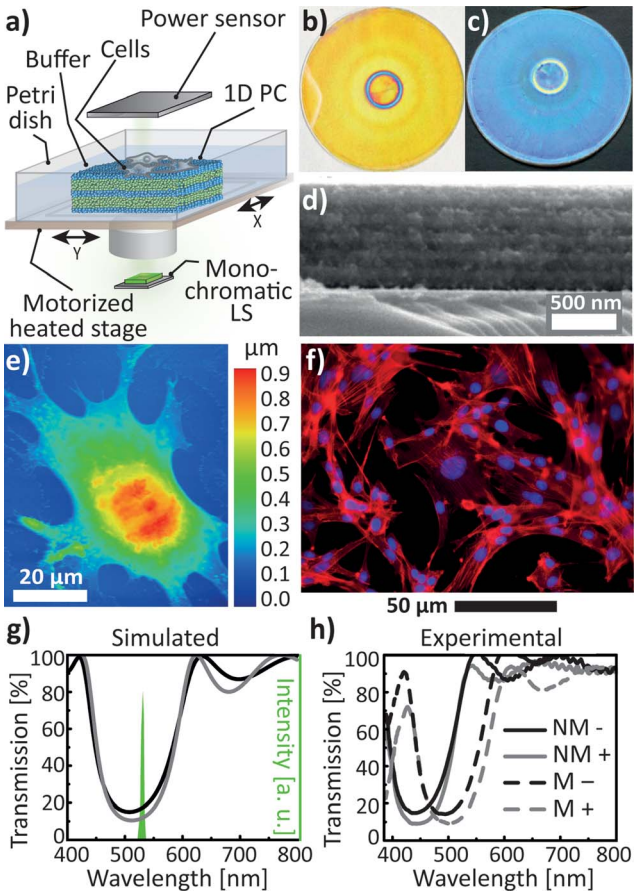

Fig. 5 (a) Schematic illustration of the photonic-to-electronic platform for cellular sensing: a 1D PC is placed into a buffer solution in the Petri dish and covered with cells, and the modulated power of the monochromatic LS is recorded by the power sensor. The photographs of the employed 1D PC taken normally (b) and approximately at 45° (c) to the PC surface (the diameter of the round substrate is 5 cm); (d) cross-section SEM image of a 1D PC composed of 6 nanoparticle-based SiO_2 (≈90 nm)/TiO_2 (≈60 nm) bilayers. (e) AFM topography of the fixed BHK-21 fibroblast cell on a 1D PC, and (f) fluorescence image of BHK-21 attached to the 1D PC after 24 h of incubation showing the distribution of F-actin and nuclear DNA inside the cells. (g) Simulated transmission spectra of the 1D PC PBG show a decrease in transmission by 8% from a PC with no cells on top (black curve) to a PC covered with a 200 nm thick cell layer (gray curve), leading to a decrease in the emission intensity of a 532 nm laser (green spectrum). (h) Experimental transmission spectra of the 1D PC PBG measured in various milieus: in air (solid lines indicated by "NM"), in cell medium (dashed lines indicated by "M"), without a cell layer (indicated by "-") and with a 100% confluent cell layer (indicated by "+").

experimental results demonstrate a decrease of 8% in the transmittance at 532 nm upon introducing the cell layer. Hence, we have shown that adding an additional "defect" cell layer on the surface of a 1D PC leads to a decrease in the output light intensity of the monochromatic light source.

Cell adhesion is known for playing a substantial role in progression and metastasis of cancer cells and is crucial for establishing new tumors in the body, hence methods for visualising proliferation or apoptosis/necrosis of cancer cells is of great interest. Therefore, we have tested the 1D-PC-based electrophotonic platform for studying the behaviour of a common liver cancer – a human hepatocellular carcinoma HuH7. Hepatocytes represent an established *in vitro* cell culture system for studies of drug metabolism, drug–drug interactions, enzyme induction and others. Our electrophotonic platform was used first for monitoring the HuH7 cell death induced by the addition of a detergent. Sodium dodecyl sulphate (SDS) is known for its ability to provide a fast (of the order of seconds) cell lysis due to the denaturation of the cell proteins and membranes.[48] The platform was integrated with the 532 nm laser and the power sensor as a detector. We have tested the robustness of the setup by measuring a low laser power baseline drift (≈1%) by a Si power meter for a bare 1D PC upon illumination with the laser (output power of 94.5 ± 0.2 μW) for several hours. Herein, the settling time of the power meter (on the order of 10–20 s) – the time difference between the moment of opening the laser shutter and the time of achieving the steady state – was also taken into account. In Fig. 6a we show the power response for a "control" 1D PC (without a HuH7 cell monolayer placed into the cell medium) to the addition of 100 μL of 1.5% aq. SDS three times at intervals indicated by the vertical arrows. The drops of the laser power seen on the curves are due to the momentary turbulence of the medium upon adding the SDS dose at 162, 231 and 300 s with a micropipette after the starting point of the experiment. As can be seen, the initial power signal of 94.5 ± 0.2 μW does not significantly change throughout the control test. On the contrary, a distinct behavior was observed for the 1D PC with a confluent HuH7 cell monolayer incubated for 48 hours (see Fig. 6b) for the same experimental procedure as for the "control" measurement (the stages of the SDS-induced cell lysis are schematically illustrated in Fig. 6c). Firstly, it is noteworthy that the initial laser power (before adding SDS) for the 1D PC with a cell layer is 6% smaller than the "control" value, and is equal to 88.7 ± 0.2 μW. Upon adding apiece 100 μL of 1.5% aq. SDS three times in the instants indicated by the vertical arrows (60, 150 and 210 s) in Fig. 6b, the signal gradually increases until it reaches the plateau value of 94.3 ± 0.2 μW. Notably, this output laser power value is identical to the one corresponding to the bare 1D PC in the "control" experiment, as indicated by the red dashed arrow in Fig. 6b, and, moreover, is in agreement with the simulation prediction of 7% decrease in transmittance due to the addition of a cell layer (see Fig. 5g). Additional characterisation of the 1D PC by widefield light microscopy in the transillumination mode, done before and after the treatment of the sample with SDS, is shown in Fig. 6d and e. Clearly, these two photographs also confirm the detachment of the cell monolayer due to the SDS-induced lysis.

Another demonstration of a non-invasive cell monitoring by our 1D-PC-based electrophotonic platform was performed *via* the real-time "visualisation" of the cell coverage on a PC surface. A schematic illustration of the performed experiment is depicted in Fig. 7a: a change in the power signal of a 532 nm laser was recorded during a slow scanning of a 1D PC hybrid with a partial cell coverage in buffer with the motorized *XY*-stage. The laser signal was measured by means of a power meter. The 1D PC partially covered with adhered HuH7 cells, incubated in a Petri

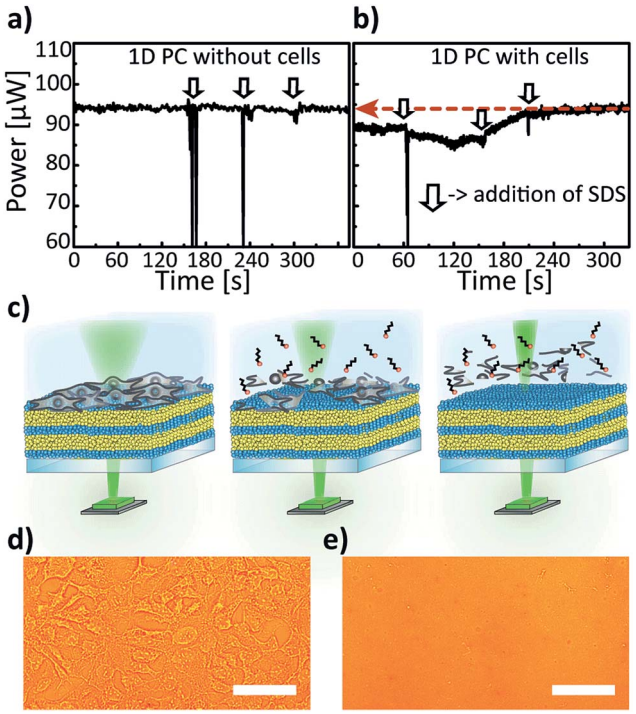

Fig. 6 (a and b) Monitoring of SDS-induced cell lysis with the 1D-PC-platform integrated with a 532 nm laser as LS and a power sensor as a detector: measurement of the power response for a laser shining through (a) a control 1D PC without a cell monolayer and (b) the 1D PC modified on top with a 100% confluent HuH7 cell layer upon adding to both systems 100 μL of 1.5% aq. SDS three times (as indicated by vertical arrows in (a and b). (c) Schematic illustration of the SDS-induced cell lysis electrophotonic experiment shown above in (b). Left: the PC covered with cells before adding SDS, middle: 0.5 min after adding SDS, right: 2.5 min after the SDS addition. (d) Photograph of the HuH7 cell monolayer, adhered to a 1D PC surface, captured in the transillumination mode before adding SDS and (e) after adding SDS (100 μL, 1.5%) three times; scale bar = 20 μm.

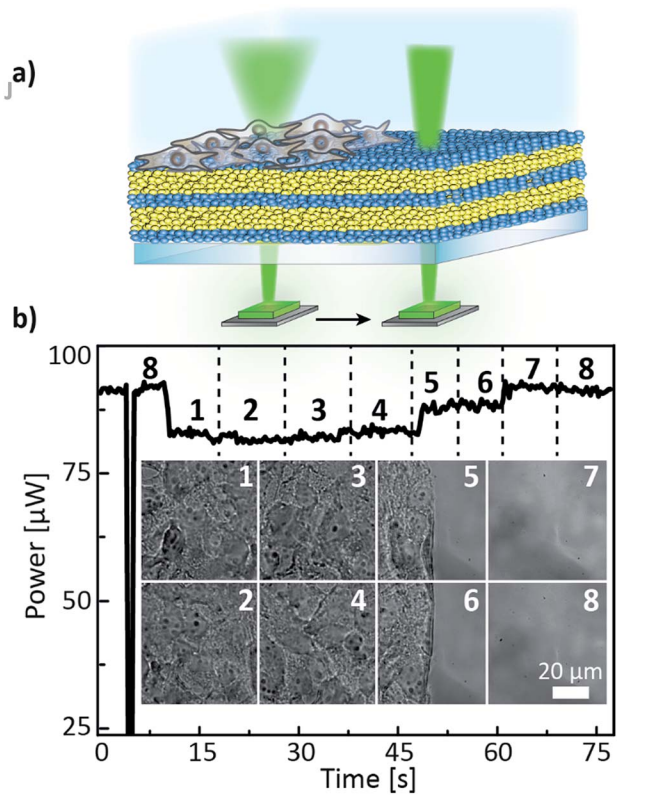

Fig. 7 (a) Schematic illustration of the cell coverage experiment, (b) laser power signal obtained during scanning the partially covered 1D PC with a HuH7 cell monolayer in the positions 1–8 with a microscope stage; the black dashed lines mark the time instants of the stage position change; the inset of Fig. 7b shows the corresponding wide-field microscope images taken in the positions 1–8.

dish in a cell medium for 24 hours, was scanned in the positions P1–P8 in a "snake-like" fashion: P8 → P1 → P2 → P3 → P4 → P5 → P6 → P7 and back to the initial position P8. The insets in the Fig. 7b show the corresponding widefield microscope images taken in the positions 1–8 with 60× magnification. Evidently, positions 1 through 4 can be characterised by a 100% confluent cell state, positions 5 and 6 by ≈50%, and positions 7 and 8 by 0% confluency. The corresponding laser power signal displays a behavior consistent with the microscope images (Fig. 7b): in the beginning of the P8 scan the power value of 90.6 ± 0.1 μW is in agreement with the previously obtained value (94.5 ± 0.2 μW) for the PC without the cell layer from the "control" measurement (see Fig. 6a). Subsequently, when the stage is brought to fully-covered P1–P4), the corresponding power value drops, and for each position it is equal to 82.1 ± 0.1 μW (decreases by 9.4%); then, in the half-covered P5 and P6 the value again increases to 88.0 ± 0.1 μW, and by bringing the laser to the bare area of the PC (P7 and P8) the signal returns to the initial value of 90.6 ± 0.2 μW. Hence, we see an agreement between the confluency state of the cell monolayer and the laser power signal. The demonstrated electrophotonic analysis of the cell cluster coverage can be of interest for cancer progression studies and for drug toxicity and pathogenicity tests.

Conclusions

In this contribution we have presented a comprehensive study harnessing the capabilities of distinct sensing functionalities and design modes of a generic 1D-PC-based electrophotonic detection platform incorporating various light emitting and detecting devices. We have demonstrated that integrating 1D PCs with narrowband light sources allows for a maximum diversity of sensing modes including the combination of spectral and intensity tuning with image processing and a straightforward photonic-to-electronic transduction scheme. We have shown the capability of the platform to spatially map the relative pressure distribution of a volatile analyte during mass transfer processes including diffusion, evaporation, droplet spreading and imbibition of porous multilayers with micrometre resolution, enabling potential applications as imaging sensors with low power consumption, straightforward assembly methods and low fabrication costs. Furthermore, based on the integration of a 1D PC with a monochromatic light source we have proposed a label-free, non-invasive platform for

in situ cell observation, which provides a complementary technique for monitoring changes in the cell motility and viability, important for applications such as the analysis of cell proliferation and differentiation, wound healing, cytotoxicity and drug screening.

Acknowledgements

This work was supported by the Max Planck Society, the University of Munich (LMU), the cluster of excellence "Nanosystems Initiative Munich" (NIM) as well as the Center for NanoScience (CeNS). We thank Prof. Bein and B. Rühle for providing access to an optical tensiometer and V. Duppel, S. M. Asano, D. G. Selmeczi (SOPRA) and R. Zenke for experimental assistance.

References

1 Y. Zhao, X. Zhao and Z. Gu, *Adv. Funct. Mater.*, 2010, **20**, 2970.
2 I. B. Burgess, M. Lončar and J. Aizenberg, *J. Mater. Chem. C*, 2013, **1**, 6075.
3 H. Xu, P. Wu, C. Zhu, A. Elbaz and Z. Z. Gu, *J. Mater. Chem. C*, 2013, **1**, 6087.
4 M. S. Luchansky and R. C. Bailey, *Anal. Chem.*, 2012, **84**, 793.
5 J. D. Joannopoulos, P. R. Villeneuve and S. Fan, *Nature*, 1997, **386**, 143.
6 C. Fenzl, T. Hirsch and O. S. Wolfbeis, *Angew. Chem., Int. Ed.*, 2014, **53**, 3318.
7 K. P. Raymond, I. B. Burgess, M. H. Kinney, M. Lončar and J. Aizenberg, *Lab Chip*, 2012, **12**, 3666.
8 D. R. Walt, *ACS Nano*, 2009, **3**, 2876.
9 D. Gallegos, K. D. Long, H. Yu, P. P. Clark, Y. Lin, S. George, P. Nath and B. T. Cunningham, *Lab Chip*, 2013, **13**, 2124.
10 A. T. Exner, I. Pavlichenko, B. V. Lotsch, G. Scarpa and P. Lugli, *ACS Appl. Mater. Interfaces*, 2013, **5**, 1575.
11 D. Psaltis, S. R. Quake and C. Yang, *Nature*, 2006, **442**, 381.
12 M. C. Estevez, M. Alvarez and L. M. Lechuga, *Laser Photonics Rev.*, 2012, **6**, 463.
13 A. T. Exner, I. Pavlichenko, D. Baierl, M. Schmidt, G. Derondeau, B. V. Lotsch, P. Lugli and G. Scarpa, *Laser Photonics Rev.*, 2014, **8**(5), 726.
14 T. A. Dickinson, J. White, J. S. Kauer and D. R. Walt, *Nature*, 1996, **382**, 697.
15 J.-W. Oh, W.-J. Chung, K. Heo, H.-E. Jin, B. Y. Lee, E. Wang, C. Zueger, W. Wong, J. Meyer, C. Kim, S.-Y. Lee, W.-G. Kim, M. Zemla, M. Auer, A. Hexemer and S.-W. Lee, *Nat. Commun.*, 2014, **5**, 3043.
16 A. Yildirim, F. E. Ozturk and M. Bayindir, *Anal. Chem.*, 2013, **85**(13), 6384.
17 I. B. Burgess, L. Mishchenko, B. D. Hatton, M. Kolle, M. Lončar and J. Aizenberg, *J. Am. Chem. Soc.*, 2011, **133**, 12430.
18 I. B. Burgess, N. Koay, K. P. Raymond, M. Kolle, M. Lončar and J. Aizenberg, *ACS Nano*, 2012, **6**, 1427.
19 S. Dhanekar and S. Jain, *Biosens. Bioelectron.*, 2013, **41**, 54.
20 L. M. Bonanno and E. Segal, *Nanomedicine*, 2011, **6**, 1755.
21 C. Pacholski, M. Sartor, M. J. Sailor, F. Cunin and G. M. Miskelly, *J. Am. Chem. Soc.*, 2005, **127**, 11636.
22 M. P. Schwartz, A. M. Derfus, S. D. Alvarez, S. N. Bhatia and M. J. Sailor, *Langmuir*, 2006, **22**, 7084.
23 I. I. Ivanov, V. A. Skryshevsky, T. Serdiuk and V. Lysenko, *Sens. Actuators, B*, 2012, **174**, 521.
24 T. L. Kelly, A. Garcia Sega and M. J. Sailor, *Nano Lett.*, 2011, **11**, 3169.
25 S. M. Shamah and B. T. Cunningham, *Analyst*, 2011, **136**, 1090.
26 E. A. Lidstone, V. Chaudhery, A. Kohl, V. Chan, T. Wolf-Jensen, L. B. Schook, R. Bashir and B. T. Cunningham, *Analyst*, 2011, **136**, 3608.
27 W. Chen, K. D. Long, M. Lu, V. Chaudhery, H. Yu, J. S. Choi, J. Polans, Y. Zhuo, B. A. C. Harley and B. T. Cunningham, *Analyst*, 2013, **138**, 5886.
28 Y. Nazirizadeh, J. Reverey, U. Geyer, U. Lemmer, C. Selhuber-Unkel and M. Gerken, *Appl. Phys. Lett.*, 2013, **102**, 011116.
29 M. E. Calvo, S. Colodrero, N. Hidalgo, G. Lozano, C. López-López, O. Sánchez-Sobrado and H. Míguez, *Energy Environ. Sci.*, 2011, **4**, 4800.
30 F. M. Hinterholzinger, A. Ranft, J. M. Feckl, B. Rühle, T. Bein and B. V. Lotsch, *J. Mater. Chem.*, 2012, **22**, 10356.
31 I. Pavlichenko, A. T. Exner, M. Guehl, P. Lugli, G. Scarpa and B. V. Lotsch, *J. Phys. Chem. C*, 2012, **116**, 298.
32 B. V. Lotsch, C. B. Knobbe and G. A. Ozin, *Small*, 2009, **5**, 1498.
33 S. Y. Choi, M. Mamak, G. von Freymann, N. Chopra and G. A. Ozin, *Nano Lett.*, 2006, **6**, 2456.
34 (*a*) S. Colodrero, M. Ocaña, A. R. González-Elipe and H. Míguez, *Langmuir*, **24**(9), 4430; (*b*) S. Colodrero, M. Ocaña, A. R. González-Elipe and H. Míguez, *Langmuir*, 2008, **24**(16), 9135.
35 Z. Wu, D. Lee, M. F. Rubner and R. E. Cohen, *Small*, 2007, **3**, 1445.
36 L. D. Bonifacio, G. A. Ozin and A. C. Arsenault, *Small*, 2011, **7**, 3153.
37 L. D. Bonifacio, B. V. Lotsch, D. P. Puzzo, F. Scotognella and G. A. Ozin, *Adv. Mater.*, 2009, **21**, 1641.
38 C. López-López, S. Colodrero, S. R. Raga, H. Lindström, F. Fabregat-Santiago, J. Bisquert and H. Míguez, *J. Mater. Chem.*, 2012, **22**, 1751.
39 E. J. Anglin, L. Cheng, W. R. Freeman and M. J. Sailor, *Adv. Drug Delivery Rev.*, 2008, **60**, 1266.
40 R. Dou and B. Derby, *Langmuir*, 2012, **28**(12), 5331.
41 T. Gambaryan-Roisman, *Curr. Opin. Colloid Interface Sci.*, 2014, **19**(4), 320.
42 K. S. W. Sing, D. H. Everett, R. A. W. Haul, L. Moscou, R. A. Pierotti, J. Rouquerol and T. Siemieniewska, *Pure Appl. Chem.*, 1985, **57**, 603.
43 V. M. Starov, S. A. Zhdanov, S. R. Kosvintsev, V. D. Sobolev and M. G. Velarde, *Adv. Colloid Interface Sci.*, 2003, **104**, 123.
44 M. Moloney, L. McDonnell and H. O'Shea, *Ultramicroscopy*, 2004, **100**, 153.
45 http://www.comsol.com/.
46 J. Bereiter-Hahn, *J. Cell Biol.*, 1979, **82**, 767.
47 N. Massad-Ivanir, G. Shtenberg, T. Zeidman and E. Segal, *Adv. Funct. Mater.*, 2010, **20**, 2269.
48 R. B. Brown and J. Audet, *J. R. Soc. Interface*, 2008, **5**(2), S131.

